International Journal of Heat and Mass Transfer 130 (2019) 1016–1031

Contents lists available at ScienceDirect

International Journal of Heat and Mass Transfer

journal homepage: www.elsevier.com/locate/ijhmt

# Numerical modeling of hot gas ingestion into the rotor-stator disk cavities of a subscale 1.5-stage axial gas turbine

Masoud Ghasemian [a,*], Marko Princevac [a], Yong W. Kim [b], Hans D. Hamm [b]

[a] Department of Mechanical Engineering, University of California, Riverside, CA 92521, USA
[b] Solar Turbines Incorporated, San Diego, CA, USA

ARTICLE INFO

*Article history:*
Received 6 July 2018
Received in revised form 16 October 2018
Accepted 29 October 2018
Available online 12 November 2018

*Keywords:*
Computational Fluid Dynamic
Gas turbine
Ingestion
Turbulence modeling
Rotor-stator disk cavity

ABSTRACT

Both steady and unsteady Reynolds Averaged Navier-Stokes (RANS) techniques coupled with the $k-\varepsilon$ and $k-\omega$ $(SST)$ turbulence models are utilized to study the flow characteristics and hot gas ingestion through rim seal in a subscale 1.5-stage axial gas turbine. A scalar transport equation is solved for a tracer gas to represent the coolant flow interaction with the main stream flow. To validate the numerical methodology, radial pressure and sealing effectiveness distributions are compared with the experimental data. The $k-\omega$ $(SST)$ turbulence model has the capability to predict secondary flow characteristics, reattachment and separation, thus leading to better agreement with the experimental data. Both radial and circumferential pressure distributions are analyzed to get deeper insight into rotationally and externally induced ingress mechanisms. The circumferential pressure peak-to-trough amplitude is significantly attenuated in the cavity region compared to annulus region. Finally, different purge flow rates and rotational speeds are examined. Results indicate that as purge flow rate increases, the static pressure in the disk cavity region raises remarkably and consequently the sealing effectiveness improves. Averaged sealing effectiveness in the rim cavity decreases linearly with the rotational speed. To visualize different mechanisms of ingestion, streamline and flow field are shown.



## 1. Introduction

In recent years, there has been a growing attention to improve the gas turbine thermal efficiency. One way to improve the overall efficiency is to increase the gas temperature at the turbine inlet. Thus, the gas turbine inlet temperature (TIT) for most gas turbines has risen to about 2000 K [1,2]. This hot gas passes through vanes and blades in the turbine annulus section and may get ingested into the disk cavity between the rotor and stator disks. As a result, overheating of turbine internal parts may occur, consequently reducing the turbine's lifetime. Hot gas ingestion from the main annulus into the wheel-space can be *Externally Induced* (EI) and *Rotationally Induced* (RI) ingress [3]. The flow through the stationary vanes and rotating blades in the turbine annulus creates a circumferential pressure asymmetry. This pressure variation causes ingress in higher pressure regions and leads to egress in lower pressure regions. This mechanism of ingestion is referred to as *Externally Induced* (EI) ingress. The other mechanism for hot gas ingestion is due to "disk pumping" effects. The rotating fluid in the wheel-space creates a radial pressure gradient. Due to centrifugal forces, fluid moves radially outward in the rotor boundary layer. To conserve radial mass flow, ingress of external fluid through the rim seal occurs in the stator boundary layer. This mechanism of ingestion is referred to as *Rotationally Induced* (RI) ingress.

Hot gas ingestion is typically mitigated or even eliminated by employing a rim seal located between rotor-stator disk or by the supply of purge flow being bled from the compressor. However, excessive use of purge air leads to a reduction in gas turbine efficiency. On the other hand, insufficient supply of purge air results in higher ingestion, which overheats the rotor disk. Therefore, it is necessary to optimize the purge flow amount assigned to the disk cavities in order to decrease aerodynamic loss.

Many experimental and computational studies have been devoted to understanding the mainstream hot gas ingestion mechanisms and the flow pattern in gas turbine rim seal region. Early experiments on the rotationally induced ingestion without considering external flow were conducted by Bayley and Owen [4], Phadke and Owen [5,6], Owen and Phadke [7] and Bhavnani et al. [8]. They proposed correlations which relate the minimum dimensionless purge flow rate necessary to prevent ingestion to the clearance and rotational Reynolds number.

* Corresponding author.
*E-mail address:* mghas002@ucr.edu (M. Ghasemian).

https://doi.org/10.1016/j.ijheatmasstransfer.2018.10.136
0017-9310/

**Nomenclature**

| | |
|---|---|
| $D_\varphi$ | molecular diffusion coefficient ($m^2/s$) |
| $D_t$ | turbulent mass diffusivity ($m^2/s$) |
| $k$ | turbulence kinetic energy ($m^2/s^2$) |
| $\dot{m}$ | purge flow rate (kg/s) |
| $r$ | radial coordinate (m) |
| $Sc_t$ | turbulent Schmidt number |
| $t$ | time (s) |
| $x$ | coordinate component |
| $y^+$ | non-dimensional distance from the wall |

*Greek letters*

| | |
|---|---|
| $\alpha$ | circumferential location at outer shroud |
| $\beta$ | circumferential location at vane platform |
| $\gamma$ | circumferential location at disk cavity |
| $\varepsilon$ | turbulent dissipation rate ($m^2/s^3$) |
| $\eta$ | sealing effectiveness |
| $\mu$ | dynamic viscosity of air (kg/m s) |
| $\rho$ | density of air ($kg/m^3$) |
| $\varphi$ | tracer gas concentration |
| $\omega$ | specific turbulence dissipation rate ($s^{-1}$) |
| $\Omega$ | rotational speed (rpm) |

*Abbreviations*

| | |
|---|---|
| CFD | Computational Fluid Dynamic |
| cfm | cubic feet per minute |
| *RANS* | Reynolds Averaged Navier-Stokes |
| rpm | revolutions per minute |
| *SST* | shear stress transport |
| *URANS* | unsteady RANS |

Phadke and Owen [9] and Dadkhah et al. [10] investigated the effect of asymmetric external flow on the sealing performance of a shrouded rotor-stator system. The minimum sealing flow rate necessary to prevent ingestion was correlated with the seal clearance and the maximum circumferential pressure difference in the annulus flow.

Balasubramanian et al. [11] measured time-averaged static pressure distribution and ingestion of main gas into the disk cavity of a subscale single-stage axial turbine equipped with an axially overlapping radial-clearance seal at the disk cavity rim and a labyrinth seal radially inboard. Their objective was to estimate the empirical discharge coefficients, based on an orifice model, over a range of purge flow rates. Moreover, the minimum purge flow rate required for the fully sealed condition was estimated. Cho et al. [12] ran experimental measurements using infrared sensors to quantify the effect of ingress on both the stator and rotor disks in a wheel-space pressurized by sealing flow. Here, the sealing effectiveness on the rotor was significantly higher than the one on the stator. Their measurements identified a so-called *thermal buffering effect*, where the sealing air attaches itself to the rotor disk. Therefore, it reduces the entrainment of ingested fluid into the disk rotor boundary layer. Palafox et al. [13] measured the sealing effectiveness of a 1.5-stage turbine wheal-space hot gas ingestion rig (HGIR). Sangan et al. [14] measured the pressure, a tracer gas concentration, and swirl for an axial turbine stage to assess the performance of two seals: a datum double-rim seal and a derivative with a series of radial fins. The finned seal provided an overall improved performance in both the inner and outer wheel-spaces over a wide range of purge flow rates. They concluded that the fins helped to produce solid-body rotation which reduces the circumferential pressure asymmetry and consequently improves the sealing effectiveness. The mechanism of hot gas ingestion through rim seal with rotor-mounted protrusion is investigated experimentally and theoretically by Liu et al. [15]. Cylinder protrusions in the cavity led to higher sealing efficiency. However, the experimental data indicated that the pressure difference between annulus and cavity is enlarged when protrusion is utilized in the rotor. The enhanced sealing effectiveness with increased pressure difference is contrary to the orifice model which claims that enlarged sealing effectiveness would come with pressure difference reduction. Therefore, the circumferential pressure variation due to the protrusion was introduced to the orifice model. Afterward, the effect of the amplitude, initial phase angle difference, and frequency of the cavity pressure wave, on the ingestion was theoretically analyzed. Savov et al. [16] compared single and double lip rim seal effectiveness experimentally. Their results showed that the double lip rim seal has higher sealing efficiency compared to the single one. The double lip seal had a smaller difference in seal effectiveness across the lower lip. This smaller gradient across the lower lip of the double lip seal suggested that it is less sensitive to mainstream-cavity interactions. Recent studies by Balasubramanian et al. [17], Patinios et al. [18], and Scobie et al. [19] have been focused on 1.5-stage axial gas turbines. Balasubramanian et al. [17] performed several experiments to measure the ingestion of mainstream air into the front and aft disk cavities in a subscale 1.5-stage axial air turbine. Different experiment sets with different main air flow rates, rotor speeds and purge air flow rates were examined. Scobie et al. [19] measured re-ingestion of upstream egress in a 1.5-stage gas turbine rig.

As turbine working conditions are still a bane for detailed flow measurements, Computational Fluid Dynamic (CFD) simulation is a powerful tool because it allows a better understanding of the flow pattern and gives an entire view of the complex physics underlying the ingestion phenomenon. Beretta and Malfa [20] and Poncet and Schiestel [21] considered the numerical modeling of the turbulent flow and heat transfer in different rotor-stator disk cavities. They proposed empirical correlation laws to predict the averaged Nusselt number depending on the Reynolds and Prandtl numbers and on the coolant flowrate. Poncet and Serre [22] used Large Eddy Simulation to examine the turbulent heat transfer in a rotor-stator cavity. The results showed that the turbulent Prandtl number is a decreasing function of the distance to the wall. The local Nusselt number was found to be proportional to the local Reynolds number to the power 0.7. Early CFD studies [23,24] showed that considering a sector model of gas turbine led to a discrepancy in the gas ingestion prediction which can be due to the circumferential periodicity assumption. Teuber et al. [25] and Zhou et al. [26] investigated the fluid mechanics of two different rim-seal geometries in a 3D model of a turbine stage. They calculated peak-to-trough pressure difference in the annulus, which is the main driving mechanism for ingestion. Wei and Huoxing [27] carried out a numerical investigation of the interaction between upstream cavity purge flow and main flow in low aspect ratio turbine cascade. The results showed that the purge flow changes the vortex structure in the passage and alters the cascade exit flow angle in the spanwise direction. Moreover, the increment of purge flow improves the sealing effectiveness but increases aerodynamic losses. Liao et al. [28] investigated the flow and heat transfer characteristics in a rotor-stator disk cavity using the Reynolds-averaged Navier-Stokes (RANS) equations coupled with the standard $k-\varepsilon$ turbulent model. Different secondary air flow rates and rotational Reynolds numbers were examined to determine their effects on the flow

and heat transfer. Their results showed that the heat transfer coefficient increases with the rotational Reynolds number increment. The local Nusselt number was correlated with the local rotational Reynolds number by a power law. Song et al. [29] numerically investigate the influence of purge flow on the endwall flow and heat transfer characteristics of a gas turbine blade. Moon et al. [30] investigated the effect of a rib installed in a rim seal on sealing effectiveness using three-dimensional Reynolds-averaged Navier-Stokes equations and the Spalart-Allmaras turbulence closure model. A parametric study with different heights, widths, and location of the ribs was performed. Wang et al. [31] numerically studied the flow characteristics of rim seal for the first stage in gas turbine. The influences of rim seal structures and rotational speeds on the sealing effectiveness were investigated. Their results indicated that the radial seals perform better than the axial ones in sealing effectiveness. The minimum non-dimensional sealing mass flow increases with the increase of rotational speed. Wang et al. [32] conducted a time-dependent 360 deg CFD simulation of a complete turbine stage with a rim seal and cavity. The pressure distributions, sealing effectiveness, and cavity velocity components were compared with experimental data. Their results showed complex pressure patterns that were not captured from sector model simulations. Ding et al. [33] carried out CFD simulation of 1.5-stage turbine wheel-space hot gas ingestion rig (HGIR) using the $k-\varepsilon$ turbulence model with scalable wall function. Scobie et al. [34] employed Unsteady Reynolds-averaged Navier-Stokes (URANS) simulation to study the performance of a new rim-seal concept. The new rim seal features a stator-side angel wing and two buffer cavities between outer and inner seals. The angel-wing promotes a counter-rotating vortex and the two buffer cavities attenuated the circumferential pressure asymmetries of the fluid ingested from the mainstream annulus. Mohamed et al. [35] performed an URANS simulation of a rotor-stator cavity with rotor bolts. The rotating bolts generate unsteadiness due to wake shedding. Zhang et al. [36] investigated the effects of the radial location of sealing air inlet hole and the shape of sealing air supply geometry on the flow characteristics and sealing performance of the stator-well cavity.

The objective of this study is to gain clear insight into ingestion patterns and mechanisms. The Reynolds Averaged Navier-Stokes simulations are performed to investigate the hot gas ingestion in a 1.5-stage axial gas turbine. Previous studies simplified the disk cavity geometry and neglected the tip clearance of cascade but in the current simulation, all geometry complexities and tip clearance are taken into account. Moreover, this study considers both front and aft cavities to capture the effect of rotating blades on upstream and downstream cavities. The correlation between purge flow rate and the circumferential pressure differences between the cavity and turbine annulus is investigated. CFD results are compared with experimental data and solver parameters are calibrated. Extensive simulations provide unique data for comparison between the performance of different turbulent closures such as $k-\varepsilon$ and $k-\omega$ $(SST)$ turbulence models. Both rotationally induced and externally induced ingestion mechanisms are studied. Different operating conditions such as purge flow rate and rotational speed are examined.

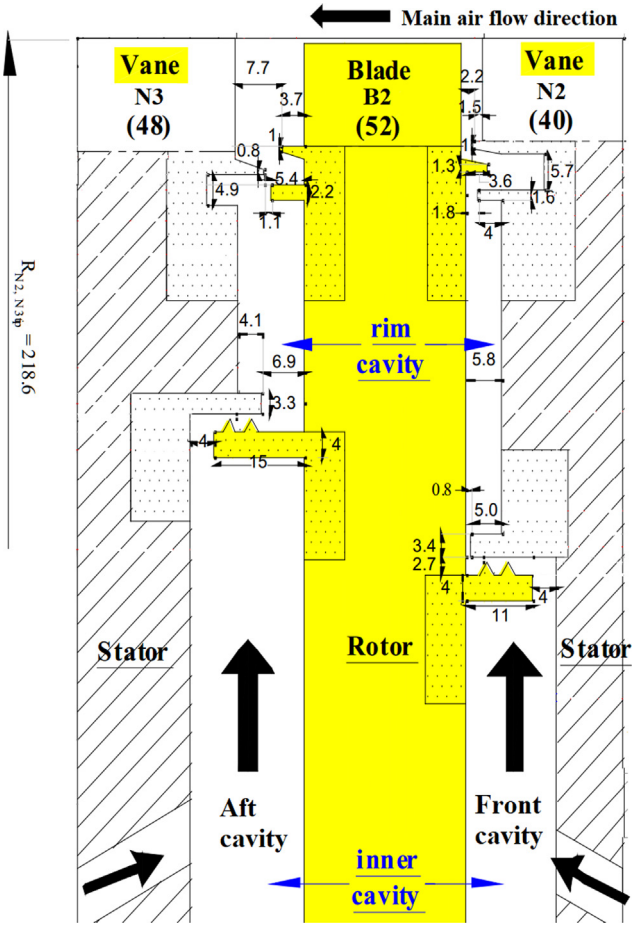


**Fig. 1.** Schematic diagram of the subscale 1.5-stage gas turbine (all dimensions are in mm) [17]. (dotted regions indicate parts that are replaceable for different test configuration.)

## 2. Problem description

The current Computational Fluid Dynamic simulations were carried out based on the gas turbine rig at Arizona State University [17]. Fig. 1 demonstrates a schematic diagram of the subscale 1.5-stage axial gas turbine. The stage design and airfoil geometries are based on an actual gas turbine of Solar Turbines Inc. The turbine features a front stator ($N_2$), a rotor ($B_2$) and an aft stator ($N_3$). The front stator ($N_2$) and aft stator ($N_3$) are equipped with 40 and 48 partial-height, full-length vanes, respectively and the rotor ($B_2$) has 52 partial-height, full-length blades.

The two disk cavities – the 'front cavity' and the 'aft cavity' – feature a radially inboard labyrinth seal which divides each disk cavity into an 'inner cavity' and a 'rim cavity'. The front rim cavity has an axially-overlapping, radial-clearance, double rim seal with a recessed buffer region. The aft rim cavity also has a recessed buffer region but also features an axial-clearance double rim seal. The

**Table 1**
ASU gas turbine rig operational condition [17].

| Rotor speed (RPM) | Flow rate | | | Static gauge pressure (Pa) | |
|---|---|---|---|---|---|
| | Main air | Front cavity purge flow | Aft cavity purge flow | Inlet | Outlet |
| 3250 | 1625 CFM [0.766915 $m^3/s$] | 6 CFM [0.00283 $m^3/s$] | 4 CFM [0.001888 $m^3/s$] | −418 | −5650.6 |

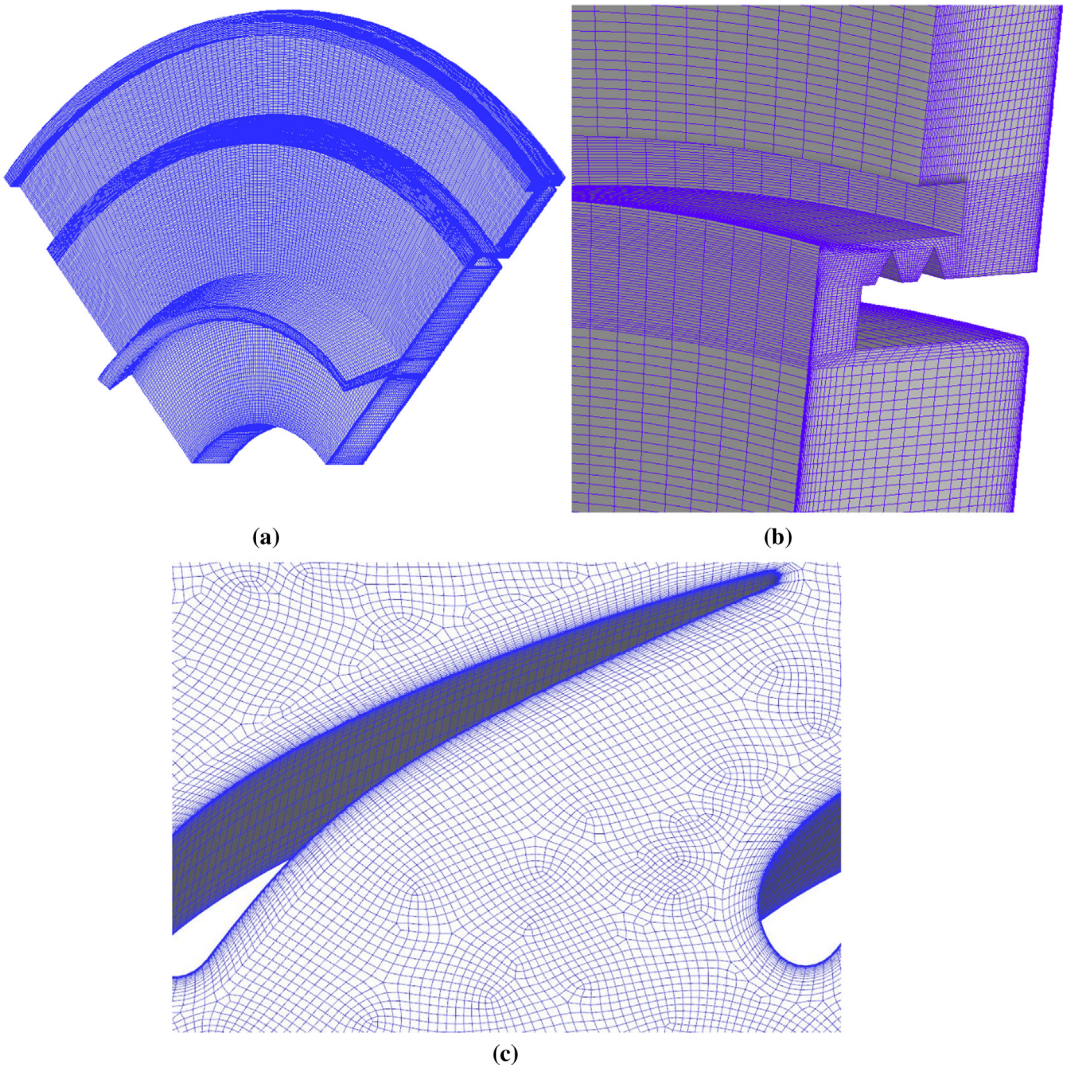


**Fig. 2.** Computational grid (a): aft disk cavity (b): labyrinth seal region (c): rotor-stator region.

stator-rotor-stator spacing and seal mimic the scaled-down dimensions of the Solar gas turbine during hot running condition.

In order to reduce the computational cost, a quarter of the gas turbine (10 $N_2$ vanes, 13 $B_2$ blades, and 12 $N_3$ vanes) is numerically simulated and periodic boundary conditions are applied to the lateral sides. The aforementioned number of vanes and blades produces a pitch ratio of 1 at the interface between $N_2$ stator, $B_2$ rotor, and $N_3$ stator. Therefore, there is no scaling approximation due to passing flow between consecutive stages with identical interfaces.

## 3. Numerical methods

The commercial CFD solver, ANSYS CFX Version 15, ANSYS Inc. [37], has been employed to solve Reynolds-Averaged Navier-Stokes (RANS) equations coupled with $k-\varepsilon$ and $k-\omega$ $(SST)$ turbulence models. A scalar equation is solved to represent the purge flow and to determine the rim sealing effectiveness. The computational domain comprises one quarter of whole gas turbine. The interaction between rotor and stator is accounted by a frozen rotor interface for steady simulations and a sliding mesh technique for unsteady simulations. Total pressure and static pressure boundary conditions are imposed to the gas mainstream inlet and outlet, respectively. Turbulence intensity of

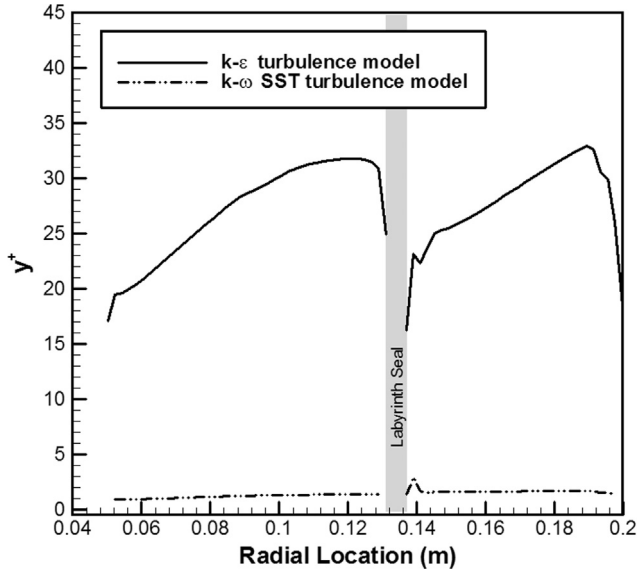


**Fig. 3.** Radial distribution of $y^+$ on the rotating surface in the front disk cavity for steady RANS simulation coupled with $k-\varepsilon$ and $k-\omega$ $(SST)$ turbulence models.

I = 10% is imposed at the inlet. Mass flow rate boundary conditions are assigned for the front and aft purge flow inlets. Rotor is assigned as a rotating domain and the other four domains ($N_2$ stator, $N_3$ stator, front cavity and aft cavity) are considered as stationary domain. High resolution, second order backward Euler, and first order upwind schemes are used for advection term, temporal and turbulence modeling, respectively. The Gauss's divergence theorem and finite-element shape functions are utilized to evaluate the control volume gradients. The residual target is that the normalized root mean square (RMS) errors for each conservation balance over the entire mesh fell to less than $10^{-5}$. The value for different boundary conditions are adapted from ASU rig data [17] and are listed in Table 1.

### 3.1. Tracer gas modeling

An additional advection-diffusion equation is solved for a passive tracer gas to visualize the ingestion phenomenon:

$$\frac{\partial}{\partial t}(\rho\varphi) + \frac{\partial}{\partial x_i}(\rho u_i \varphi) = \frac{\partial}{\partial x_i}\left(\left(\rho D_\varphi + \frac{\mu_t}{Sc_t}\right)\frac{\partial}{\partial x_i}\varphi\right) \quad (1)$$

where $\varphi$ is the tracer gas concentration, $D_\varphi$ is the molecular diffusion coefficient and $Sc_t = \mu_t/\rho D_t$ is the turbulent Schmidt number which is the ratio of turbulent viscosity and turbulent mass diffusivity. In this study, the default turbulent Schmidt number, $Sc_t = 0.9$ is employed.

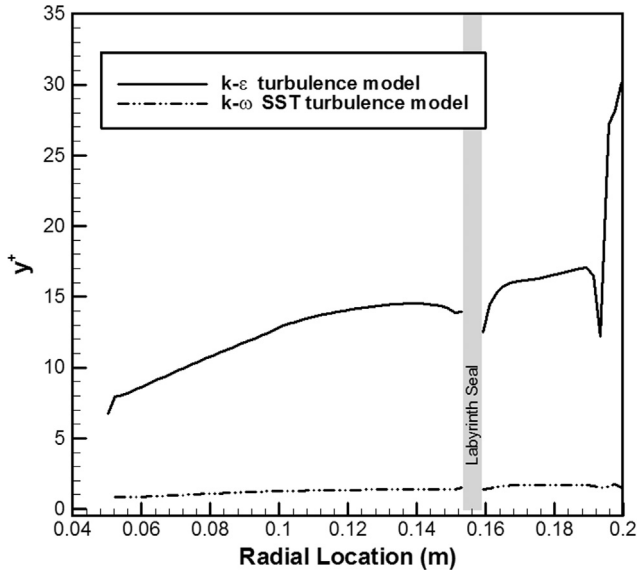


**Fig. 4.** Radial distribution of $y^+$ on the rotating surface in the aft disk cavity for steady RANS simulation coupled with $k-\varepsilon$ and $k-\omega$ (*SST*) turbulence models.

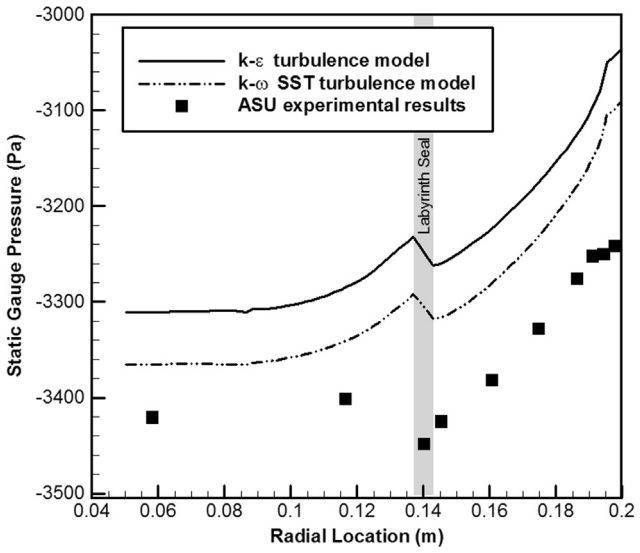


**Fig. 6.** Radial static gauge pressure distribution on the stator surface in the front disk cavity for steady RANS simulation coupled with $k-\varepsilon$ and $k-\omega$ (*SST*) turbulence models.

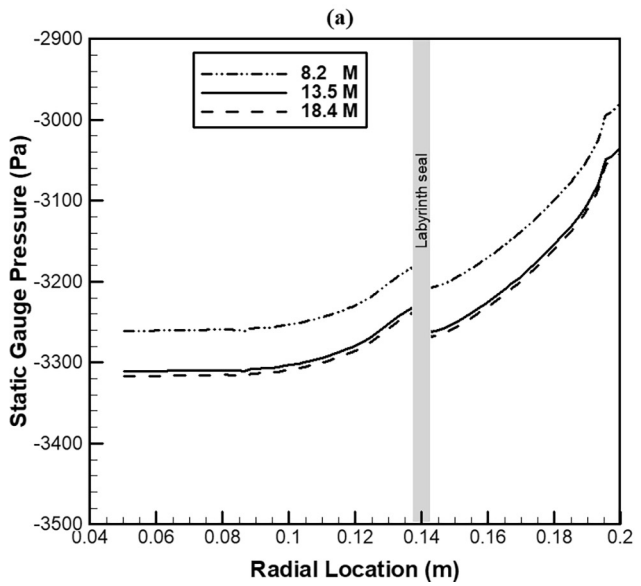


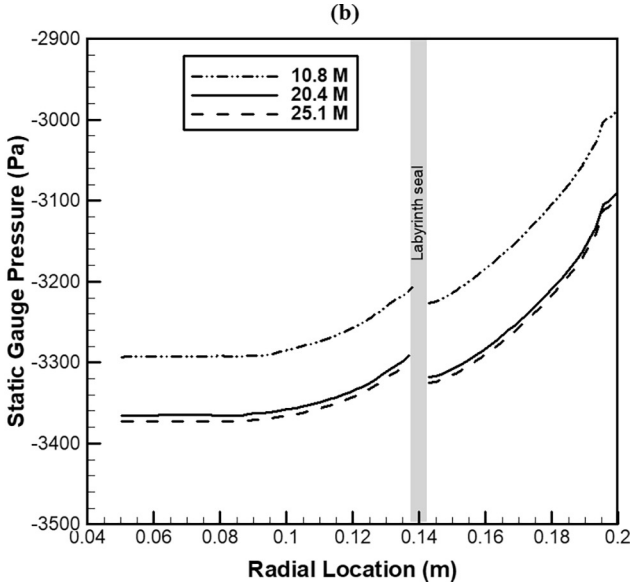


**Fig. 5.** Grid refinement study using radial pressure distribution on the stator surface in the front disk cavity for steady RANS simulation (a): $k-\varepsilon$ turbulence model. (b): $k-\omega$ (*SST*) turbulence model.

The molecular diffusion coefficient has the value of $D_{\varphi} = 1.6 \times 10^{-5}$ [m²/s]. The computed tracer gas concentrations in the purge air supply, main air inlet and disk cavities are employed to calculate a local sealing effectiveness value, $\eta(r)$, for each location of the front and aft cavities. An effectiveness value of 0 indicates zero sealing and a value of 1 indicates complete sealing.

For the front cavity:

$$\eta(r) = \frac{\varphi(r) - \varphi_{main}}{\varphi_{r=116.5\ \mathrm{mm}} - \varphi_{main}} \tag{2}$$

where $\varphi_{main}$ is tracer gas concentration in the main air inlet and $\varphi_{r=116.5\ \mathrm{mm}}$ is the tracer gas concentration in the inner cavity at the location of $r = 116.5$ [mm].

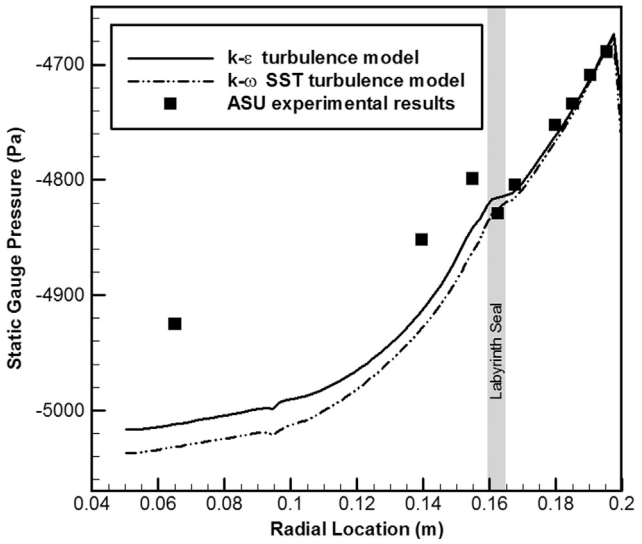


**Fig. 7.** Radial static gauge pressure distribution on the stator surface in the aft disk cavity for $k-\varepsilon$ and $k-\omega$ (*SST*) turbulence models.

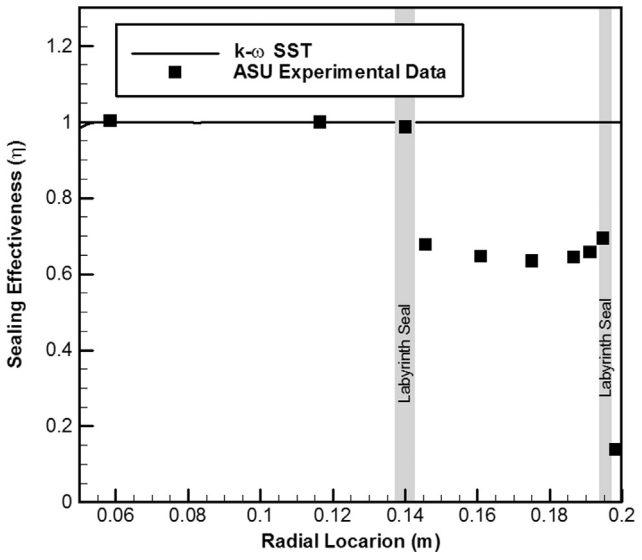


**Fig. 8.** Radial distribution of local sealing effectiveness on the stator surface in the front disk cavity computed by steady RANS simulation coupled with $k-\omega$ (SST) for $\dot{m}_{Purge} = 6$ [CFM] and $\Omega = 3250$ rpm.

For the aft cavity:

$$\eta(r) = \frac{\varphi(r) - \varphi_{main}}{\varphi_{purge} - \varphi_{main}} \tag{3}$$

where $\varphi_{purge}$ is the tracer gas concentration in the purge air flow. It should be noted that the mentioned definitions are consistent with definitions of the sealing effectiveness at ASU experiments.

### 3.2. Computational grid

The unstructured grid was generated for the annulus region while a structured grid was employed in the disk cavity regions to discretize the computational domain. The grid points are clustered close to the seals where the velocity and concentration gradients are larger. Fig. 2 presents grid distributions in the wheel-space, labyrinth seal, and main stream region. The circumferential spatial resolution for both front and aft disk cavities is equal to 1° per cell.

In this study, in order to reduce the grid number and computational cost, wall function was utilized in the wall boundary

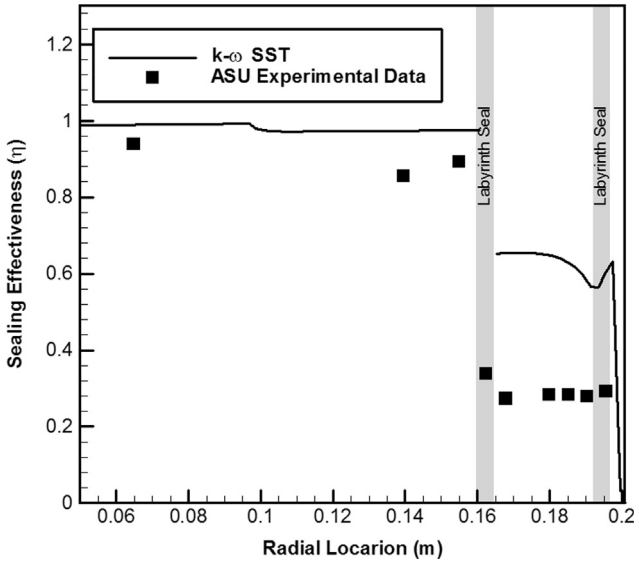


**Fig. 9.** Radial distribution of local sealing effectiveness on the stator surface in the aft disk cavity computed by steady RANS simulation coupled with $k-\omega$ (SST) for $\dot{m}_{Purge} = 4$ [CFM] and $\Omega = 3250$ rpm.

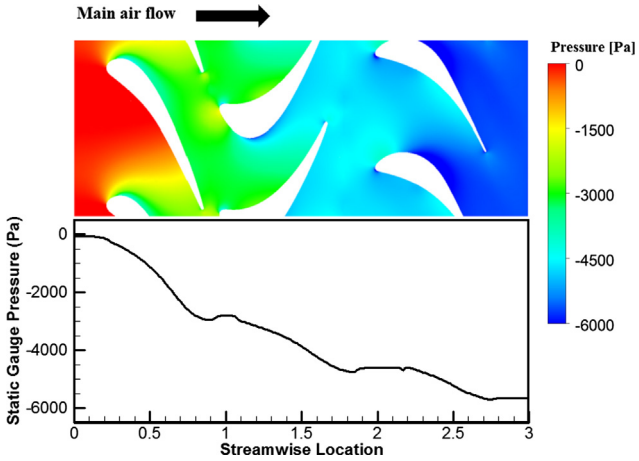


**Fig. 10.** Averaged static gauge pressure variation in the streamwise direction in the annulus section of gas turbine from the mainstream flow inlet to outlet.

conditions. Wall function is valid within a specific range of $y^+$. The $y^+$ associated with the first cell should not be too large that the first node falls outside of the log-law layer and it should not be too small that the first node is placed in the viscous sublayer of the boundary layer [38]. The scalable and automatic wall functions are deployed for the $k-\varepsilon$ and $k-\omega$ $(SST)$ turbulence models, respectively. To verify that the resolution of computational grid is consistent with wall function, $y^+$ on the cavities' walls are computed. Figs. 3 and 4 show the $y^+$ distribution on the rotating surface in the front and aft disk cavities, respectively. For the $k-\varepsilon$ turbulence model the $y^+$ is in the range of $5 < y^+ < 40$ and for the $k-\omega$ $(SST)$ turbulence model the $y^+ \cong 1$. These $y^+$ values are consistent with scalable wall function in $k-\varepsilon$ turbulence model and near wall resolution in $k-\omega$ $(SST)$, respectively.

In order to confirm the grid independency, different computational grids were tested. Fig. 5 shows the radial distribution of pressure on the stator surface in the front disk cavity. As the number of cells exceeds about 20 million and 13 million elements for $k-\omega$ $(SST)$ and $k-\varepsilon$ turbulence models, respectively, there is a negligible variation in the pressure distribution. For example, the average pressure difference between 20.4 million and 25.1 million grids is less than 8 Pa (0.2%). Therefore, we used a computational domain with 20.4 million cells for $k-\omega$ $(SST)$ turbulence model and 13.5 million cells for $k-\varepsilon$ turbulence model. This difference in the number of cells for $k-\varepsilon$ and $k-\omega$ $(SST)$ turbulence models is due to different wall functions used for each turbulence model.

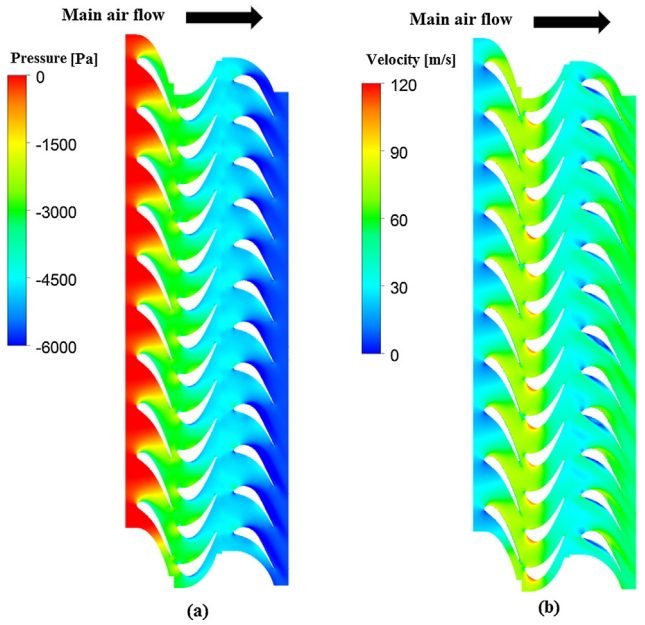


**Fig. 11.** Blade-to-Blade contour (a) static gauge pressure (b) velocity in stationary frame.

### 3.3. Methodology validation

In order to demonstrate the accuracy of the CFD methodology, pressure data acquired from CFD simulation are compared with ASU experimental rig data. The $k-\varepsilon$ and $k-\omega$ $(SST)$ shear stress transport turbulence models are applied. The $k-\varepsilon$ turbulence model computes the eddy viscosity in the RANS equations by solving two transport equations for turbulent kinetic energy and turbulent dissipation rate. This model is numerically stable and robust but it is not able to predict secondary flow characteristics, reattachment and separation. Moreover, $k-\varepsilon$ fails to correctly predict the onset and amount of separation in the adverse pressure

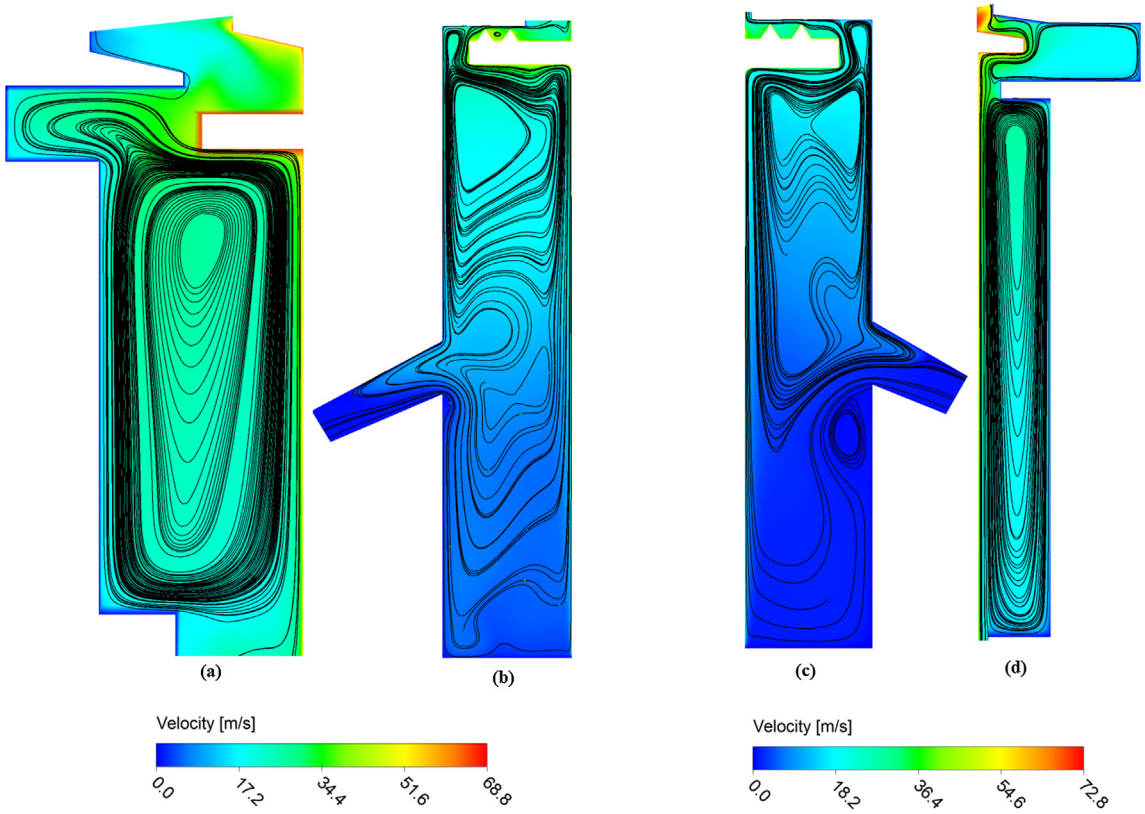


**Fig. 12.** Streamline and contour of velocity- (a) aft rim cavity- (b) aft inner cavity- (c) front inner cavity- (d) front rim cavity.

gradient flows. The $k-\omega$ $(SST)$ turbulence model is a combination of superior elements of $k-\omega$ and $k-\varepsilon$ turbulence models. It utilizes the $k-\omega$ turbulence model in the inner part of boundary layer and gradually switches to the standard $k-\varepsilon$ model in the wake region of the boundary layer and free shear layers [39]. The transition between these two models is based on a blending function. This blending function is one in the sublayer and logarithmic region of boundary layer and gradually switches to zero in the wake region and free shear layers. The other advantage of $k-\omega$ $(SST)$ turbulence model is that the eddy viscosity formulation is modified to take into account the effect of turbulent shear stress transportation. This turbulent shear stress transportation is important to predict severe adverse pressure gradient flows [40].

Fig. 6 shows the radial static gauge pressure distribution on the stator surface in the front disk cavity. The $k-\omega$ $(SST)$ turbulence model shows a better agreement with experimental data. This improvement can be due to the ability of this model to capture the adverse pressure gradient flow in the disk cavity region.

Fig. 7 depicts the radial static gauge pressure variation on the stator surface in the aft disk cavity. The $k-\varepsilon$ turbulence model has a slightly better prediction compared to $k-\omega$ $(SST)$ turbulence model in the inner cavity region. In the rim cavity region, both turbulence models could perfectly predict static pressure. Therefore, $k-\omega$ $(SST)$ turbulence model, due to its better agreement especially in the front disk cavity, has been chosen for future simulations. Soghe et al. [41] used two modified versions of the k-ω SST model including the curvature correction and reattachment modification. These modified versions demonstrated better capa-

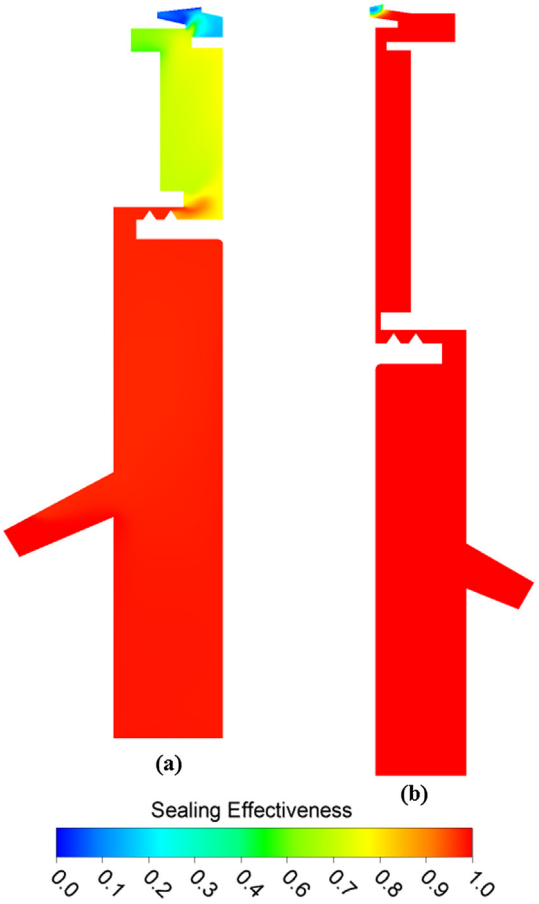


**Fig. 13.** Sealing effectiveness for front and aft disk cavities (a): aft disk cavity with $\dot{m}_{Purge} = 4$ [CFM] - (b): front disk cavity with $\dot{m}_{Purge} = 6$ [CFM].

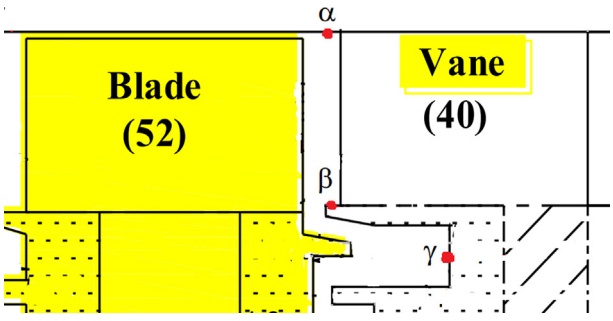


**Fig. 14.** Circumferential location for pressure distribution plots – 'α' location: 1.5 [mm] downstream $N_2$ vane trailing edge at the shroud – 'β' location: 0.6 [mm] downstream $N_2$ vane trailing edge at the hub – 'γ' location: on the $N_2$ stator surface in the front disk cavity at r = 198 [mm].

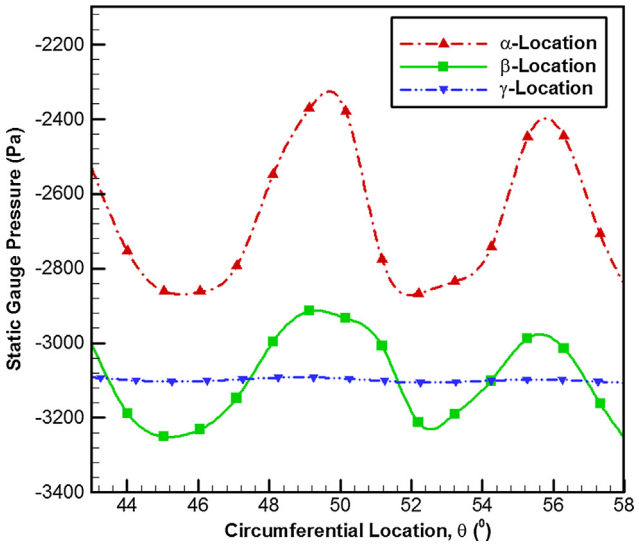


**Fig. 15.** Circumferential distribution of static gauge pressure at different locations for $\dot{m}_{purge} = 6$ [CFM].

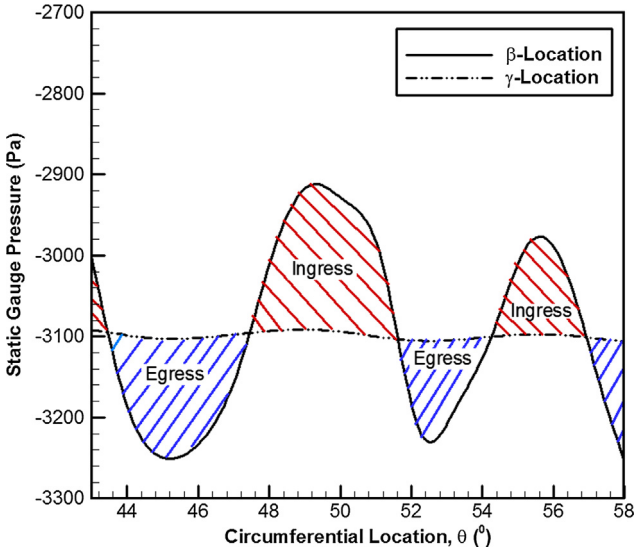


**Fig. 16.** Circumferential distribution of static gauge pressure in annulus and cavity region for $\dot{m}_{purge} = 6$ [CFM].

bilities, but standard $k-\omega$ (SST) model offered the best trade-off between accuracy and computational cost.

To evaluate the capability of CFD simulation in the prediction of rim seal ingestion, numerical sealing effectiveness for steady $k-\omega$ (SST) model were compared with the experimental data. Figs. 8 and 9 show radial distribution of local sealing effectiveness at the stator surface in the front and aft disk cavities, respectively. In contrast with pressure data validation, CFD poorly modeled ingestion and overpredicts the sealing effectiveness compared to the rig experimental data. This discrepancy is more severe in the front cavity. This overprediction can be due to employing steady simulation. It highlights that ingestion is an unsteady phenomenon and steady RANS technique is not able to capture it precisely. Therefore, authors investigate the effects of unsteadiness in Section 4.5 by employing URANS technique.

**Table 2**
Purge flow rate for aft and front disk cavities.

| Total [CFM] | Front cavity [60%] [CFM] | Aft cavity [40%] [CFM] |
|---|---|---|
| 10 | 6 | 4 |
| 20 | 12 | 8 |
| 30 | 18 | 12 |
| 40 | 24 | 16 |

## 4. Results and discussion

### 4.1. Flow and sealing effectiveness visualization

Fig. 10 shows the averaged axial static gauge pressure drop in the 1.5-stage axial gas turbine from the mainstream flow inlet to the outlet. To provide deeper insight into pressure variation, the axial pressure variation plot is shown along the pressure contour

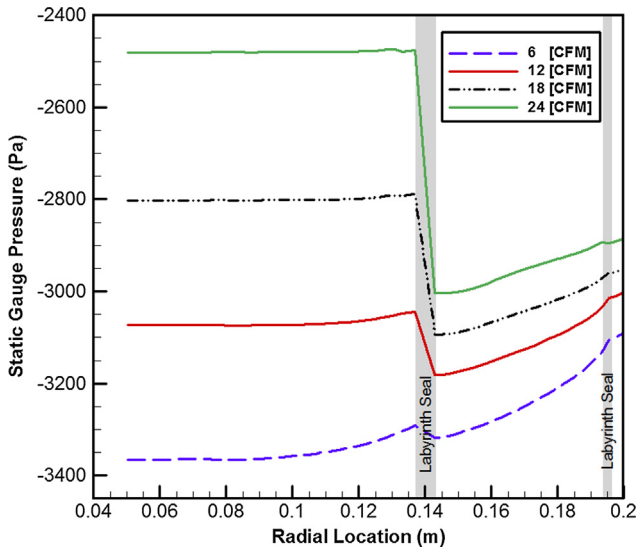


**Fig. 17.** Radial distribution of static gauge pressure on the stator surface of front cavity for different purge flow rates.

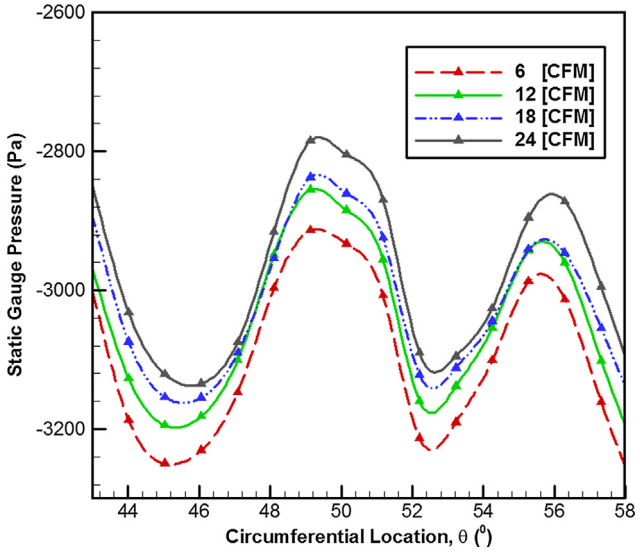


**Fig. 19.** Circumferential distribution of static gauge pressure at $\beta$ location for different purge flow rates $\dot{m}_{purge} = 6, 12, 18$ *and* 24 [CFM].

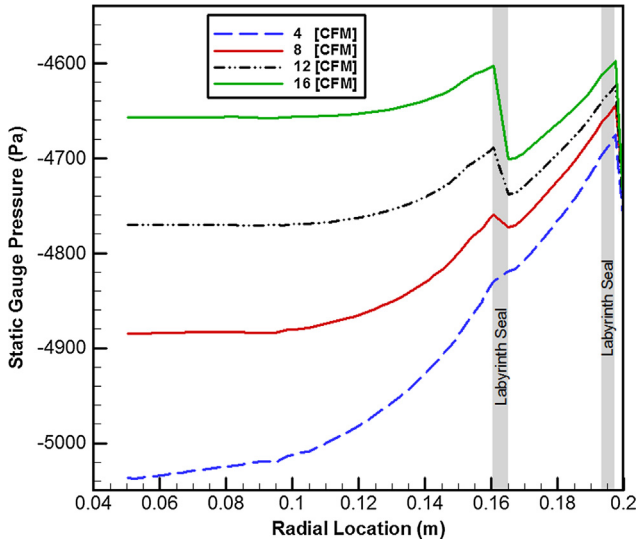


**Fig. 18.** Radial distribution of static gauge pressure on the stator surface of aft cavity for different purge flow rates.

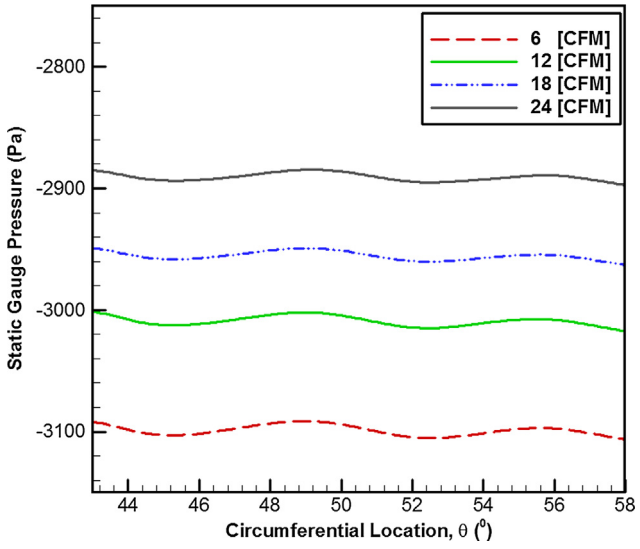


**Fig. 20.** Circumferential distribution of static gauge pressure at $\gamma$ location for different purge flow rates $\dot{m}_{purge} = 6, 12, 18$ *and* 24 [CFM].

in the annulus section of the gas turbine. It can be seen that as flow passes through vanes and blades, the static pressure drops by about 6000 [Pa] from the mainstream flow inlet to outlet, which is consistent with ASU experimental rig data.

Fig. 11 depicts the contour of static gauge pressure and velocity in the stationary frame at the gas turbine annulus section in the Blade-to-Blade view. The velocity contour shows that the maximum velocity reaches about 120 [m/s] in the region close to rotating blade leading edge and the minimum velocity occurs close to the stationary vanes leading edges.

Fig. 12 shows the contour of velocity and streamlines in front and aft disk cavities. These streamlines demonstrate the rotationally induced ingress. Fluid moves radially outward in the rotor boundary layer and inward in the stator boundary layer. Between the boundary layers, especially for the rim cavities which the flow has higher tangential velocity, a core of fluid rotates at the speed necessary to satisfy the conservation of mass. This rotation creates a radial pressure gradient which results in pressure increase with the radius.

Fig. 13 depicts the contour of local sealing effectiveness for the front and aft disk cavities. The front disk cavity is fully sealed while the aft disk cavity has inefficient sealing effectiveness. This difference between sealing effectiveness can be due to the rim seal axial overlapping in the front disk cavity and 50% more purge flow rate supplied to the front disk cavity. For the aft disk cavity, the sealing effectiveness in the rim cavity is around 0.6. The front cavity fully sealing can also be due to the substantial pressure drop across the labyrinth seal. This pressure drop resists ingestion into the inner cavity. Sealing effectiveness comparison between front and aft disk cavities shows that the rim seal axial overlapping had a key role in mitigating the hot gas ingestion.

### 4.2. Circumferential pressure asymmetry

In order to show circumferential pressure asymmetry, static gauge pressure is plotted at three different circumferential locations: at 1.5 [mm] downstream of $N_2$ vane trailing edge on the outer shroud ($\alpha$ location), at 0.6 [mm] downstream of $N_2$ vane

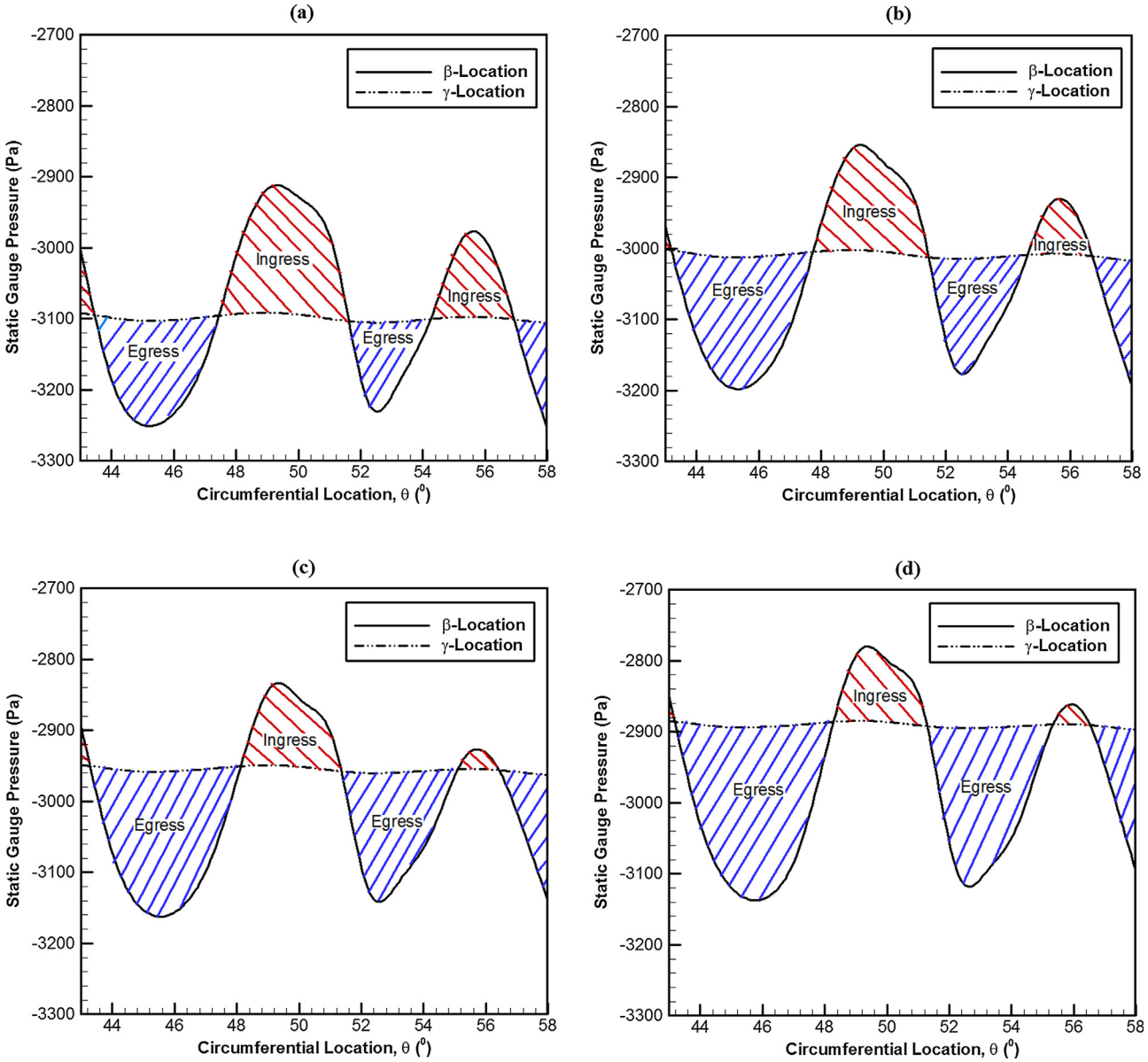


**Fig. 21.** Circumferential distribution of static gauge pressure in annulus and cavity region for different purge flow rates $\dot{m}_{purge} = 6, 12, 18$ *and* 24 [CFM].

trailing edge on the hub ($\beta$ location), and on the $N_2$ stator surface in the front disk cavity at r = 198 [mm] ($\gamma$ location). These locations are illustrated in Fig. 14.

Fig. 15 shows the circumferential variation of static gauge pressure at $\alpha$, $\beta$, and $\gamma$ circumferential locations over two $N_2$ vane pitches. The pressure wave pattern varies from one pitch to another and it is due to the pitch difference between $N_2$ vanes and $B_2$ blades. At each circumferential location, pressure variations show the same phase but different amplitudes. The pressure level at the outer shroud region is higher compared to the vane platform pressure and it can be due to the centrifugal force imposed by rotation. Among the three locations, the maximum peak-to-trough

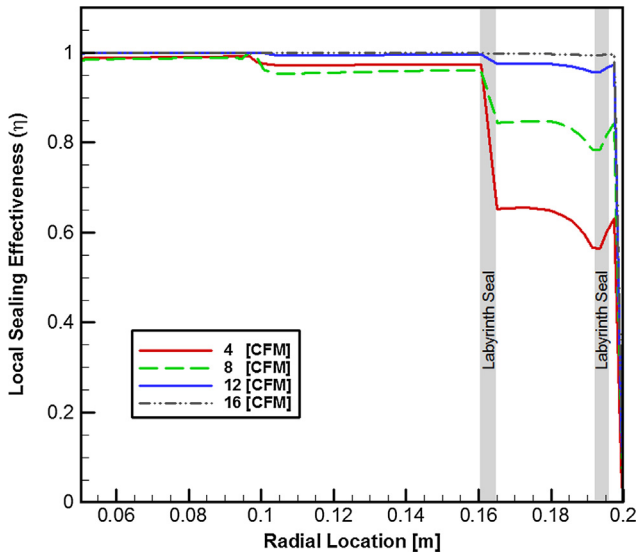


**Fig. 22.** Radial distribution of sealing effectiveness on the stator surface of aft disk cavity for different purge flow rates $\dot{m}_{purge} = 4, 8, 12$ *and* 16 [CFM].

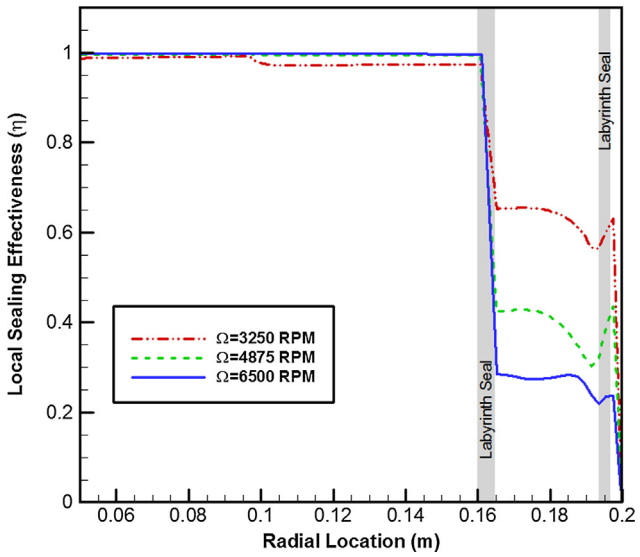


**Fig. 24.** Radial variation of sealing effectiveness on stator surface of aft disk cavity for different rotational speeds $\Omega = 3250, 4875,$ and 6500 rpm and $\dot{m}_{Purge} = 4$ [CFM].

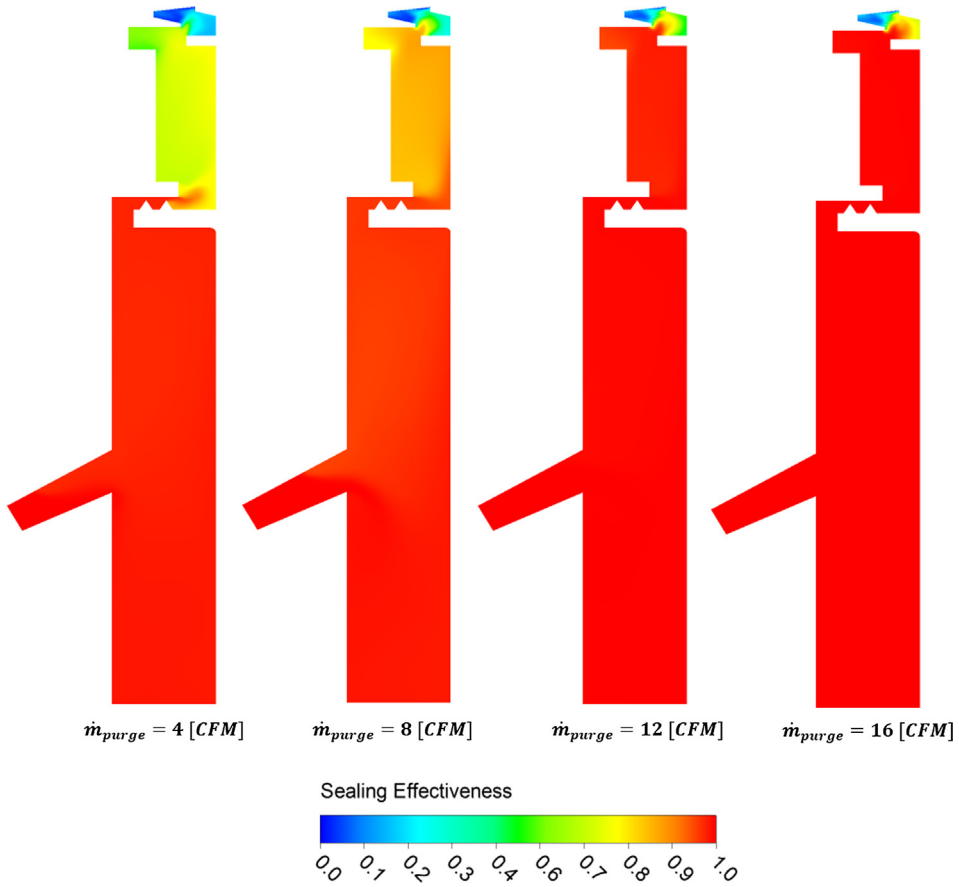


**Fig. 23.** Contour of local sealing effectiveness in the aft disk cavity for different purge flow rates $\dot{m}_{purge} = 4, 8, 12$ *and* 16 [CFM].

amplitude occurs at the $\alpha$ location and the peak-to-trough amplitude decreases by marching toward the vane platform and it is significantly attenuated in the cavity region. The pressure peak-to-trough amplitude is about 550 [Pa] and 300 [Pa] at the $\alpha$ and $\beta$ locations, respectively.

As mentioned, when flow passes through stationary vanes and rotating blades, it creates regions of low and high pressure. This pressure asymmetry causes ingress in higher pressure regions and leads to egress in lower pressure regions. The pressure at the outer shroud ($\alpha$ location) is influenced by the blade tip flow and has less relevance to the rim seal gas ingestion compared to the pressure close to the vane platform ($\beta$ location). Therefore, $\beta$ location was chosen to analyze externally induced ingestion. Fig. 16 shows ingress and egress regions based on the pressure difference between annulus and cavity region. The solid line with larger peak-to-trough amplitude stands for annulus pressure and the dash line with smaller peak-to-trough amplitude stands for pressure in the cavity region. Ingress occurs in the regions where annulus pressure is higher than the cavity pressure and egress takes place where the pressure of annulus is lower than the cavity pressure.

### 4.3. Effects of purge flow rate

This section focuses on the effect of purge flow rate on the pressure and sealing effectiveness distribution in radial and circumferential directions. Four different purge flow rates were examined as listed in Table 2.

Figs. 17 and 18 show the radial distribution of static gauge pressure for different purge flow rates at stator surface in the front and aft disk cavities, respectively. As the purge flow rate increases, the pressure level in the inner cavity raises about 900 [Pa] and 400 [Pa] in the front and aft disk cavities, respectively. This remarkable pressure ascent is due to the flow restriction imposed by the labyrinth seal. Moreover, there is higher pressure drop in the labyrinth seal for higher purge flow rates. This higher-pressure drop will result in higher sealing effectiveness. The radial pressure gradient in the rim cavity is higher than the inner cavity which can lead to steeper variation in the sealing effectiveness in the rim cavity. This difference in the pressure gradient is due to higher tangential velocity and centrifugal force in the rim cavity compared to the inner cavity.

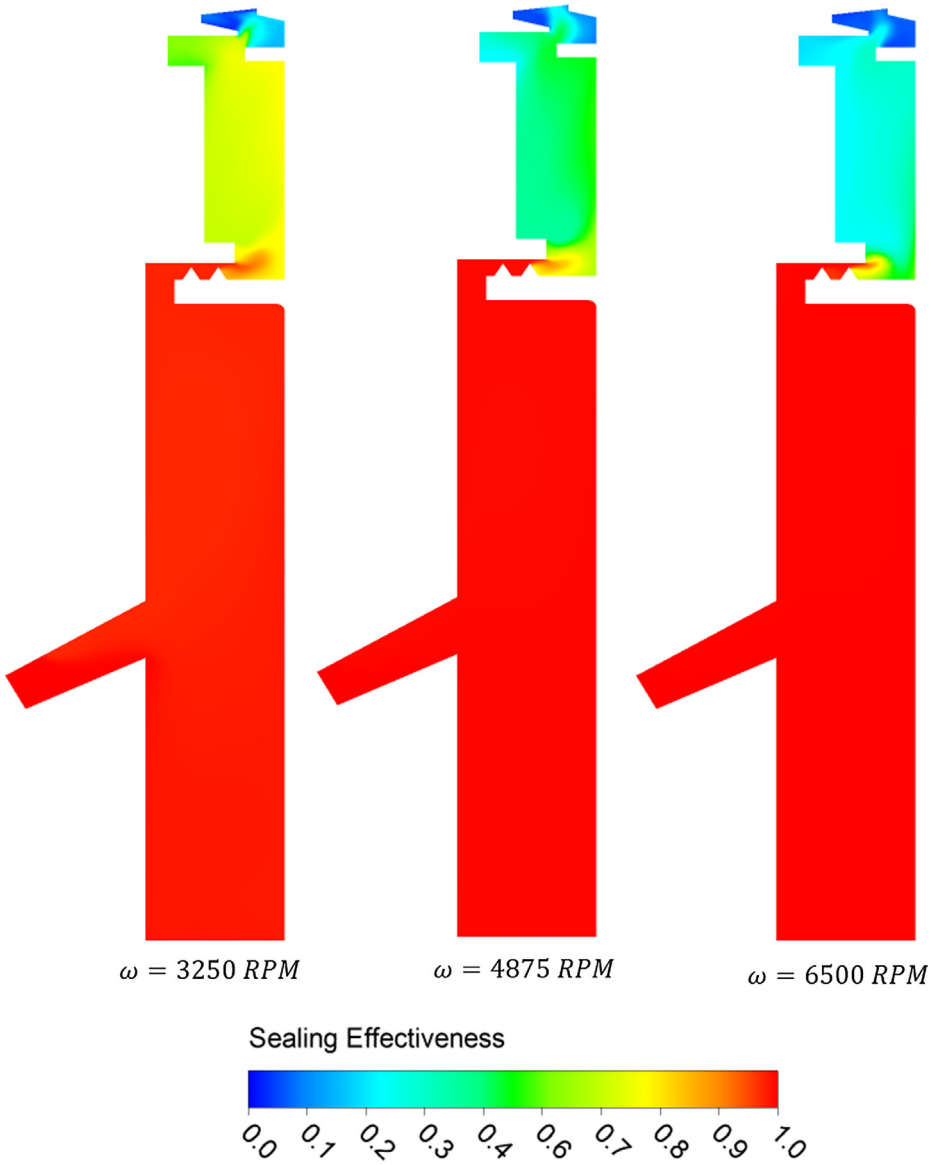


**Fig. 25.** Contour of local sealing effectiveness in the aft cavity for different rotational speeds $\Omega = 3250, 4875,$ and 6500 rpm and $\dot{m}_{Purge} = 4$ [CFM].

Fig. 19 shows the circumferential variation of static gauge pressure at $\beta$ location, 0.6 [mm] downstream of $N_2$ vane trailing edge on the vane platform, for four different purge flow rates $\dot{m}_{purge} = 6, 12, 18$ *and* 24 [CFM]. As the purge flow rate increases from 6 [CFM] to 24 [CFM], the pressure increases around 130 [Pa]. Change in the purge flow rate does not alter the pressure wave phase and the peak-to-trough pressure amplitude remains approximately unchanged for different purge flow rates, but the whole pressure curve shifts upward with purge flow rate.

Fig. 20 shows the circumferential distribution of static gauge pressure at $\gamma$ location, on the $N_2$ stator surface in the front disk cavity at r = 198 [mm], for four different purge flow rates $\dot{m}_{purge} = 6, 12, 18$ *and* 24 [CFM]. The peak-to-trough pressure asymmetry amplitude at $\gamma$ location is significantly small compared to the $\beta$ location. As the purge flow rate increases from 6 [CFM] to 24 [CFM], the pressure level at $\gamma$ location raises by 210 [Pa].

Fig. 21 shows both circumferential pressure distribution in $\beta$ and $\gamma$ locations and differential areas between them, which determines ingress and egress regions for different purge flow rates. As the purge flow rate increases, the pressure in both cavity and annulus regions shift upward. The pressure inside the cavity is more sensitive to the purge flow rate variations. Therefore, it would have higher raise with purge flow rate. Our results show that when the purge flow rate increases from 6 [CFM] to 24 [CFM], the averaged up-shift is about 210 [Pa] and 130 [Pa] for the cavity and annulus region, respectively. It means that increase in the purge flow rate leads to egress area increment and ingress area reduction. Consequently, it mitigates mainstream flow ingestion into the disk cavity region. This indicates that the purge flow rate can alter the pressure field and influence the hot gas ingestion due to circumferential pressure asymmetry.

Fig. 22 shows the radial distribution of local sealing effectiveness on the stator surface of the aft cavity for different purge flow rates $\dot{m}_{purge} = 4, 8, 12$ *and* 16 [CFM]. For all purge flow rates, the inner cavity is approximately fully sealed. However, the rim cavity region is more sensitive to the purge flow rate and the sealing effectiveness increases from 0.6 to 1 for purge flow rates from 4 to 16 [CFM]. The sealing effectiveness consistently improved with purge flow.

Fig. 23 depicts the contour of local sealing effectiveness in the aft disk cavity for different purge flow rates $\dot{m}_{purge} = 4, 8, 12$ *and* 16 [CFM]. Higher purge flow rates result in higher sealing effectiveness. This trend is compatible with pressure drop seen in Fig. 18. As Fig. 23 illustrates, there is a fully sealed condition in the purge flow rate of 16 [CFM]. Therefore, this amount of purge flow is enough to prevent ingestion in the aft disk cavity.

### 4.4. Effects of rotational speed

This section highlights the influence of rotational speed on rim seal ingestion. Three different rotational speeds $\Omega = 3250$, 4875, and 6500 rpm were examined. Fig. 24 shows the radial distribution of local sealing effectiveness on the stator surface of the aft disk cavity. As it was expected, the sealing effectiveness decreases with the increase of the rotational speed. Higher rotational speeds lead to higher centrifugal forces which increase the pressure difference between annulus and cavity region and consequently rotationally induced ingestion. In the higher rotational speeds, the

**Table 3**
Solver parameters for URANS simulation.

| Time step (s) | Total time | Iteration per time step | Convergence criteria |
|---|---|---|---|
| $2.3 \times 10^{-5}$ | 5 Revolutions | 10 | RMS residual less than $10^{-5}$ |

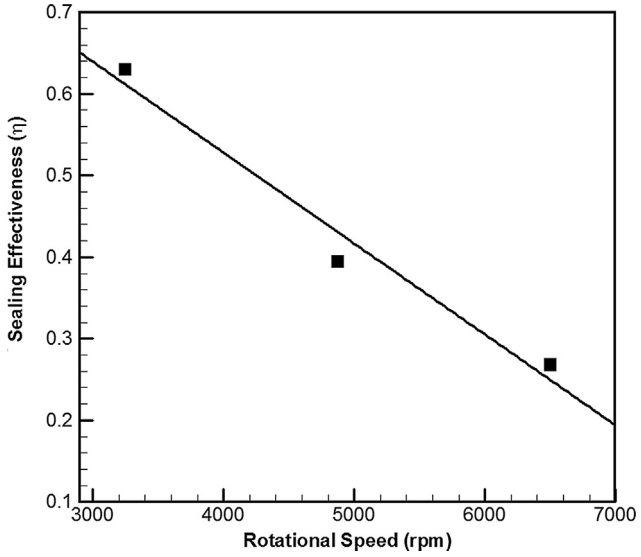


**Fig. 26.** Variation of averaged sealing effectiveness in the rim cavity with rotational speed for $\dot{m}_{Purge} = 4$ [CFM].

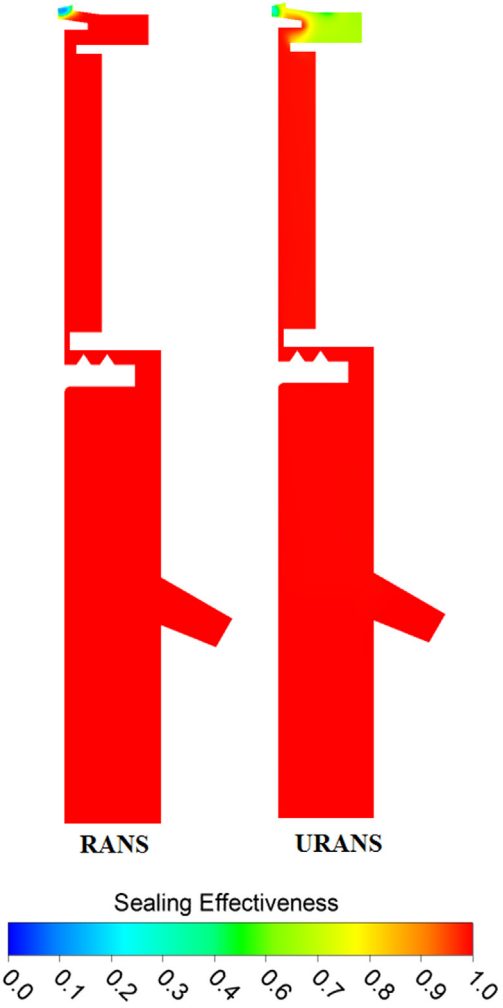


**Fig. 27.** Contour of sealing effectiveness in the front disk cavity for both RANS and URANS simulations.

rotationally induced ingestion mechanism is the dominant mechanism compared to the externally induced ingress mechanism.

Contours of local sealing effectiveness for different rotational speeds are shown in Fig. 25. Rotational speed has a negligible effect on the local sealing effectiveness of the inner cavity, but the sealing effectiveness decreases with rotational speed in the rim cavity. For instance, 50% increase in rotational speed leads to a 37% reduction in the averaged sealing effectiveness in the rim cavity region.

In order to show the correlation between the sealing effectiveness and rotational speed, the averaged values of local sealing effectiveness on the aft stator surface in the rim cavity region for different rotational speeds were calculated and the variation of the averaged sealing effectiveness versus rotational speed is shown in Fig. 26. The averaged sealing effectiveness decreases approximately in a linear trend with respect to the rotational speed, which is consistent with [4,5]. According to [4,5], the minimum dimensionless flow rate necessary to prevent ingress varies linearly with the rotational Reynolds number. The minor discrepancy between our results and the linear relationship can be attributed to the inclusion of mainstream annulus in the current study. Refs. [4,5] conducted their experiments without the main gas path and it is possible that such an external flow could change the relation between the sealing effectiveness and rotational speed.

### 4.5. Effects of unsteadiness

The unsteady Reynolds averaged Navier-Stokes (URANS) simulation has been carried out to consider the rotor-stator unsteady effects on the hot gas ingestion into rotor-stator disk cavities. The solver parameters have been listed in Table 3.

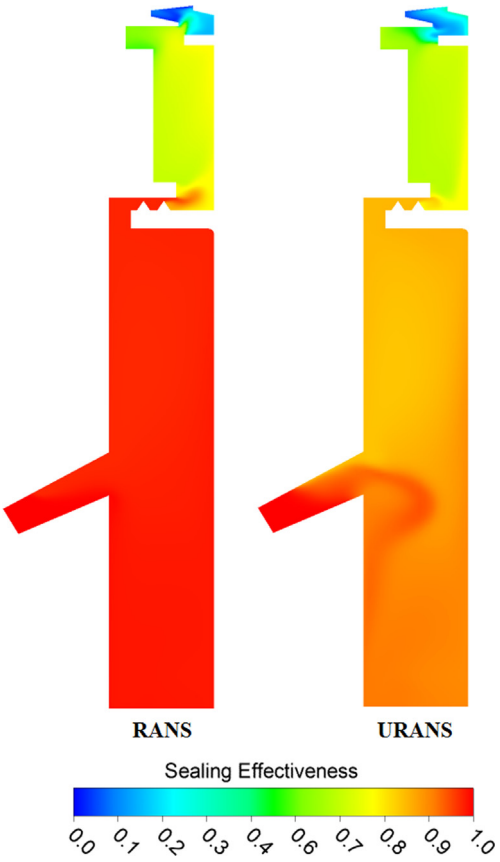


**Fig. 28.** Contour of sealing effectiveness in the aft disk cavity for both RANS and URANS simulations.

Fig. 27 shows the contour of local sealing effectiveness in the front disk cavity for both RANS and URANS simulations. Although URANS technique predicts lower sealing effectiveness close to the rim seal compared to the RANS technique, both approaches overpredicted the sealing effectiveness compared to the rig data. The URANS results demonstrate that the unsteady effects led to more hot gas ingestion into the disk cavity but still there is a deviation in the ingestion amount in comparison with the experimental data. The unsteady effects are even more pronounced in the aft cavity.

The contour of local sealing effectiveness in the aft disk cavity for both RANS and URANS simulations have been shown in Fig. 28. Similar to the front disk cavity, the URANS simulation predicted higher ingestion into the disk cavity, especially into the inner disk cavity.

The radial distribution of sealing effectiveness on the stator surface for the front and aft disk cavities has been shown in

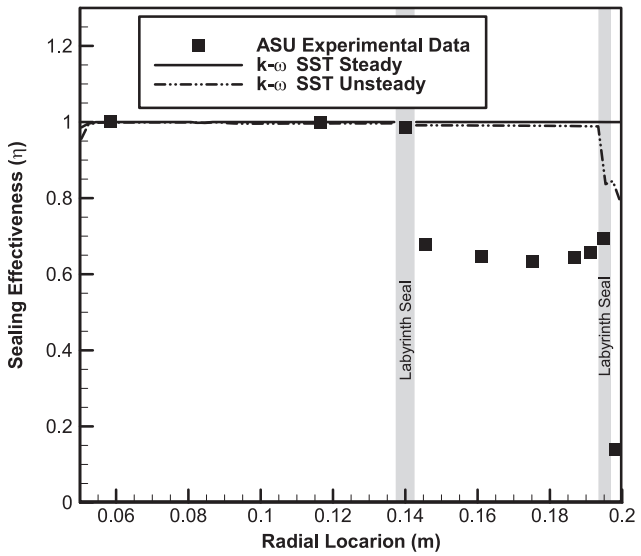


**Fig. 29.** Local sealing effectiveness on the stator surface of the front disk cavity for both RANS and URANS simulations.

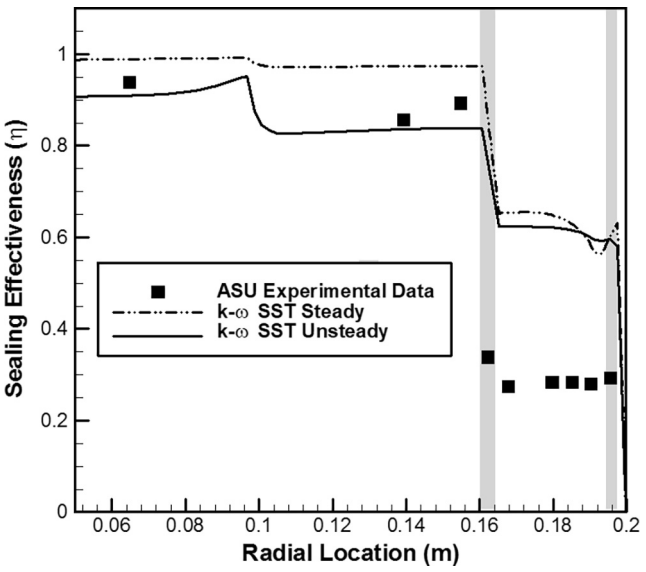


**Fig. 30.** Local sealing effectiveness on the stator surface of the aft disk cavity for both RANS and URANS simulations.

Figs. 29 and 30. For the aft cavity, steady RANS approach predicted a fully sealed condition in the inner cavity, while the sealing effectiveness varies around 0.8 in the unsteady RANS simulation. Both RANS and URANS approaches predicted the sealing effectiveness of 0.6 through the rim cavity which is higher than the rig data.

## 5. Conclusion

In the current study, numerical simulations were conducted to investigate the flow characteristics and rim seal gas ingestion in a subscale 1.5-stage gas turbine. The numerical methodology has been validated against experimental data. Also, radial and circumferential distributions of pressure were analyzed within annulus and wheel-space. Both rotationally and externally induced ingestion mechanisms were studied under different purge flow rates and rotational speeds. The principal conclusions that can be drawn are as follows:

- Steady Reynolds Averaged Navier-Stokes approach can predict the pressure distribution correctly, but it underpredicts hot gas ingestion and overpredicts sealing effectiveness. This overprediction motivated unsteady simulations (URANS). The URANS predicted lower sealing effectiveness, however, still above the experimental results.
- The URANS approach could predict sealing effectiveness correctly for inner cavities, but there is overprediction in rim cavities.
- The $k-\omega$ $(SST)$ turbulence model, due to its superiority in predicting secondary flow characteristics, reattachment and separation, leads to better results compared to the $k-\varepsilon$ turbulence model. However, $k-\omega$ $(SST)$ turbulence model required larger grid cell number because of its near wall resolution scheme.
- Streamlines in the wheel-space display an outward flow in the $B_2$ rotor disk boundary layer and an inward flow in the $N_2$ and $N_3$ stator disks boundary layers. This flow pattern is a proof of rotationally induced ingress mechanisms.
- As the purge flow rate increases, the static pressure in both inner and rim disk cavities increases, but this raise is more remarkable in the inner cavity. The pressure gradient is larger in the rim cavity compared to the inner cavity. This difference can be attributed to higher tangential velocity and centrifugal force in the rim cavity.
- As the purge flow rate increases, circumferential pressure has higher shift-up in the cavity compared to the annulus. Therefore, it decreases the ingress regions and increases the egress regions. Consequently, the sealing effectiveness is improved.
- The front disk cavity has better sealing effectiveness compared to aft disk cavity. That can be due to the rim seal axial overlapping in the front disk cavity.
- As the rotational speed increases, the sealing effectiveness in the rim cavity reduces. The averaged sealing effectiveness on the stator surface decreases linearly with rotational speed.

## Conflict of interest

The authors declared that there is no conflict of interest.

## Acknowledgments

The authors gratefully acknowledge the financial support provided by the Solar Turbines Inc. for this project.

## References

[1] R. Krewinkel, A review of gas turbine effusion cooling studies, Int. J. Heat Mass Transf. 66 (2013) 706–722, https://doi.org/10.1016/j.ijheatmasstransfer.2013.07.071.
[2] T. Gao, J. Zeng, J. Li, J. Gong, Numerical prediction on mist/steam cooling in a square ribbed channel at real gas turbine operational conditions, Int. J. Heat Mass Transf. 108 (2017) 1089–1102, https://doi.org/10.1016/j.ijheatmasstransfer.2016.12.094.
[3] J.A. Scobie, C.M. Sangan, J. Michael Owen, G.D. Lock, Review of ingress in gas turbines, J. Eng. Gas Turb. Power 138 (2016) 120801, https://doi.org/10.1115/1.4033938.
[4] F.J. Bayley, J.M. Owen, The fluid dynamics of a shrouded disk system with a radial outflow of coolant, J. Eng. Gas Turb. Power 92 (1970) 335–341, https://doi.org/10.1115/1.3445358.
[5] U.P. Phadke, J.M. Owen, An investigation of ingress for an 'Air Cooled' shrouded rotating disk system with radial clearance seals, ASME J. Eng. Power 105 (1983) 178–183.
[6] U.P. Phadke, J.M. Owen, Aerodynamic aspects of the sealing of gas turbine rotor-stator systems: Part 1: the behavior of simple shrouded rotating-disk systems in a quiescent environment, Int. J. Heat Fluid Flow 9 (1988) 98–105.
[7] J.M. Owen, U.P. Phadke, An investigation of ingress for a simple shrouded rotating disc system with a radial outflow of coolant, ASME 1980 Int. Gas Turbine Conf. Prod. Show, Am. Soc. Mech. Eng., 1980.
[8] S.H. Bhavnani, J.M. Khodadadi, J.S. Goodling, J. Waggot, An experimental study of fluid flow in disk cavities, J. Turbomach. 114 (1992) 454–461.
[9] U.P. Phadke, J.M. Owen, Aerodynamic aspects of the sealing of gas-turbine rotor-stator systems. Part 3: the effect of nonaxisymmetric external flow on seal performance, Int. J. Heat Fluid Flow. 9 (1988) 113–117, https://doi.org/10.1016/0142-727X(88)90062-8.
[10] S. Dadkhah, A.B. Turner, J.W. Chew, Performance of radial clearance rim seals in upstream and downstream rotor-stator wheelspaces, J. Turbomach. 114 (1992) 439–445, https://doi.org/10.1115/1.2929163.
[11] J. Balasubramanian, P.S. Pathak, J.K. Thiagarajan, P. Singh, R.P. Roy, A.V. Mirzamoghadam, Experimental study of ingestion in the rotor-stator disk cavity of a subscale axial turbine stage, J. Turbomach. 137 (2015) 1–10, https://doi.org/10.1115/1.4030099.
[12] G. Cho, C.M. Sangan, J.M. Owen, G.D. Lock, Effect of ingress on turbine discs, Proc. ASME Turbo Expo 2015 Turbine Tech. Conf. Expo. GT2015, 2015.
[13] P. Palafox, Z. Ding, J. Bailey, T. Vanduser, K. Kirtley, K. Moore, A New 1.5-stage turbine wheelspace hot gas ingestion rig (HGIR) – Part I: experimental test vehicle, measurment capability and baseline results, Proc. ASME Turbo Expo 2013 Turbine Tech. Conf. Expo. GT2013, 2013.
[14] C.M. Sangan, J.A. Scobie, J. Michael Owen, G.D. Lock, K.M. Tham, V.P. Laurello, Performance of a finned turbine rim seal, J. Turbomach. 136 (2014) 111008, https://doi.org/10.1115/1.4028116.
[15] D. Liu, Z. Tao, X. Luo, H. Wu, X. Yu, Development of a new factor for hot gas ingestion through rim seal, J. Eng. Gas Turbines Power. 138 (2015) 072501, https://doi.org/10.1115/1.4031758.
[16] S.S. Savov, N.R. Atkins, S. Uchida, Comparison of single and double lip rim seal geometry, Proc. ASME Turbo Expo 2016 Turbomach. Tech. Conf. Expo., 2016.
[17] J. Balasubramanian, M. Michael, R.P. Roy, Y.W. Kim, H.K. Moon, Experiments on front- and aft- disk cavity ingestion in a subscale 1.5-stage axial turbine, Proc. ASME Turbo Expo 2016 Turbomach. Tech. Conf. Expo. GT2016, 2016.
[18] M. Patinios, J.A. Scobie, C.M. Sangan, J.M. Owen, G.D. Lock, Measurements and modeling of ingress in a new 1.5-stage turbine research facility, J. Eng. Gas Turbines Power Trans. ASME 139 (2017), https://doi.org/10.1115/1.4034240.
[19] J.A. Scobie, F.P. Hualca, M. Patinios, C.M. Sangan, M.J. Owen, G.D. Lock, Re-ingestion of upstream egress in a 1.5-stage gas turbine rig, Proc. ASME Turbo Expo 2017 Turbomach. Tech. Conf. Expo. GT2017 June 26–30, 2017, Charlotte, NC, USA, 2017.
[20] G.P. Beretta, E. Malfa, Flow and heat transfer in cavities between rotor and stator disks, Int. J. Heat Mass Transf. 46 (2003) 2715–2726, https://doi.org/10.1016/S0017-9310(03)00065-6.
[21] S. Poncet, R. Schiestel, Numerical modeling of heat transfer and fluid flow in rotor-stator cavities with throughflow, Int. J. Heat Mass Transf. 50 (2007) 1528–1544, https://doi.org/10.1016/j.ijheatmasstransfer.2006.08.028.
[22] S. Poncet, E. Serre, High-order LES of turbulent heat transfer in a rotor-stator cavity, Int. J. Heat Fluid Flow 30 (2009) 590–601, https://doi.org/10.1016/j.ijheatfluidflow.2009.01.011.
[23] R. Jakoby, T. Zierer, K. Lindblad, J. Larsson, L. DeVito, D.E. Bohn, J. Funcke, A. Decker, Numerical simulation of the unsteady flow field in an axial gas turbine rim seal configuration, Proc. ASME Turbo Expo 2004, Power Land, Sea, Air (GT2004-53829), 2004.
[24] D.W. Zhou, R.P. Roy, C.-Z. Wang, J.A. Glahn, Main gas ingestion in a turbine stage for three rim cavity configurations, J. Turbomach. 133 (2011) 031023, https://doi.org/10.1115/1.4002423.
[25] R. Teuber, Y.S. Li, J. Maltson, M. Wilson, Computational extrapolation of turbine sealing effectiveness from test rig to engine conditions, in: Proc. ASME Turbo Expo 2012 GT2012 June 11–15, 2012, Copenhagen, Denmark, 2012, pp. 1–12.
[26] K. Zhou, M. Wilson, J.M. Owen, G.D. Lock, Computation of ingestion through gas turbine rim seals, Proc. Inst. Mech. Eng. Part G J. Aerosp. Eng. 227 (2012) 1101–1113, https://doi.org/10.1177/0954410012450229.
[27] J. Wei, L. Huoxing, Numerical investigation of the interaction between upstream cavity purge flow and main flow in low aspect ratio turbine

cascade, Chin. J. Aeronaut. 26 (2013) 85–93, https://doi.org/10.1016/j.cja.2012.12.021.
[28] G. Liao, X. Wang, J. Li, J. Zhou, Numerical investigation on the flow and heat transfer in a rotor-stator disc cavity, Appl. Therm. Eng. 87 (2015) 10–23, https://doi.org/10.1016/j.applthermaleng.2015.05.002.
[29] L. Song, P. Zhu, J. Li, Z. Feng, Effect of purge flow on endwall flow and heat transfer characteristics of a gas turbine blade, Appl. Therm. Eng. 110 (2017) 504–520, https://doi.org/10.1016/j.applthermaleng.2016.08.172.
[30] M.A. Moon, C.S. Lee, K.Y. Kim, Effect of a rib on rim seal performance, Int. Commun. Heat Mass Transf. 59 (2014) 130–135, https://doi.org/10.1016/j.icheatmasstransfer.2014.10.011.
[31] X. Wang, G. Liao, F. Zhang, J. Li, Numerical investigation on the steady and unsteady flow characteristics of rim seal for the first stage in gas turbine, Appl. Therm. Eng. 99 (2016) 11–22, https://doi.org/10.1016/j.applthermaleng.2016.01.021.
[32] C.-Z. Wang, S.P. Mathiyalagan, B.V. Johnson, G.J. Axel, D.F. Cloud, Rim seal ingestion in a turbine stage from 360-degree time-dependent numerical simulations, J. Turbomach. 136 (3) (2014) 681–693, https://doi.org/10.1115/1.4024684.
[33] Z. Ding, P. Palafox, K. Moore, R. Chupp, K. Kirtley, A new 1.5-stage turbine wheelspace hot gas ingestion rig (HGIR) – Part II: CFD modeling and validation, Proc. ASME Turbo Expo 2013 Turbine Tech. Conf. Expo. GT2013, 2013.
[34] J.A. Scobie, R. Teuber, Y.S. Li, C.M. Sangan, M. Wilson, G.D. Lock, Design of an improved turbine rim-seal, Proc. ASME Turbo Expo 2015 Turbine Tech. Conf. Expo. GT2015, June 15–19, 2015, Montr. Canada, vol. 138, 2015, pp. 1–12, https://doi.org/10.1115/1.4031241.
[35] S.N. Mohamed, J.W. Chew, N.J. Hills, Effect of bolts on flow and heat transfer in a rotor-stator disk cavity, J. Eng. Gas Turb. Power 139 (2017) 051901, https://doi.org/10.1115/1.4035144.
[36] F. Zhang, X. Wang, J. Li, D. Zheng, Numerical investigation on the effect of radial location of sealing air inlet and its geometry on the sealing performance of a stator-well cavity, Int. J. Heat Mass Transf. 115 (2017) 820–832, https://doi.org/10.1016/j.ijheatmasstransfer.2017.08.053.
[37] ANSYS CFX Version 15, ANSYS Inc., Canonsburg, PA, 2013.
[38] M. Ghasemian, Z.N. Ashrafi, A. Sedaghat, A review on computational fluid dynamic simulation techniques for Darrieus vertical axis wind turbines, Energy Convers. Manage. 149 (2017), https://doi.org/10.1016/j.enconman.2017.07.016.
[39] F.R. Menter, Two-equation eddy-eiscosity turbulence models for engineering applications, AIAA J. 32 (1994) 1598–1605, https://doi.org/10.2514/3.12149.
[40] D.A. Johnson, L.S. King, A mathematically simple turbulence closure model for attached and separated turbulent boundary layers, AIAA J. 23 (1985) 1684–1692, https://doi.org/10.2514/3.9152.
[41] R. Da Soghe, L. Innocenti, A. Andreini, S. Marta, Numerical benchmark of turbulence modeling in gas turbine rotor-stator system, Proc. ASME Turbo Expo 2010 Power Land, Sea Air, Glasgow, UK, 2010.